

**CORROSION EVALUATION OF ADDITIVE MANUFACTURE METAL ALLOY  
BY NONDESTRUCTIVE LINE-FOCUSED TRANSDUCER**

by

**Chenglong Ji**

Bachelor of Engineering, Tongji University, 2012

Submitted to the Graduate Faculty of  
Swanson School of Engineering in partial fulfillment  
of the requirements for the degree of  
Master of Science

University of Pittsburgh

2017

UNIVERSITY OF PITTSBURGH  
SWANSON SCHOOL OF ENGINEERING

This thesis was presented

by

Chenglong Ji

It was defended on

November 17, 2017

and approved by

Qing-Ming Wang, Ph.D., Professor,

Department of Mechanical Engineering and Materials Science

Patrick Smolinski, Ph.D., Associate Professor,

Department of Mechanical Engineering and Materials Science

Williams S. Slaughter, Ph.D., Associate Professor,

Department of Mechanical Engineering and Materials Science

Thesis Advisor: Qing-Ming Wang, Ph.D., Professor,

Department of Mechanical Engineering and Materials Science

Copyright © by Chenglong Ji

2017

# **CORROSION EVALUATION OF ADDITIVE MANUFACTURE METAL ALLOY BY NONDESTRUCTIVE LINE-FOCUSED TRANSDUCER**

Chenglong Ji, M.S.

University of Pittsburgh, 2017

In this study, the elastic properties of the additive manufactured and the traditional manufactured standard sample of stainless steel – grade 420 (SS420) before and after the electrochemical corrosion will be characterized by using the line-focused ultrasonic transducer system. The calculation was based on the measurement of the surface Rayleigh wave's velocity. The result showed that the velocity of the surface wave and Young's modulus had a negative correlation with the degree of corrosion, which means as the degree of the corrosion became severer, the velocity of the surface wave and Young's modulus decreased. A galvanic cell to simulate the electrochemical corrosion in this test was established and a concave transducer with a motorized stage was used to emit and detect the ultrasonic waves which could be used in surface wave's calculation.

This thesis research includes four parts: 1) theoretical consideration of the surface wave propagating and the elastic constants in an isotropic material; 2) basic principles and procedures of the measurement regarding the surface Rayleigh wave and the corrosion evaluation; 3) data processing and the result of Young's modulus variation with regards to the corrosion; 4) the conclusions about this experiment and some future expectations.

## TABLE OF CONTENTS

<b>NOMENCLATURE.....</b>	<b>X</b>
<b>ACKNOWLEDGEMENT.....</b>	<b>XII</b>
<b>1.0 INTRODUCTION.....</b>	<b>1</b>
<b>1.1 CURRENT VESSEL CORROSION TEST METHOD .....</b>	<b>1</b>
<b>1.2 MOTIVATION.....</b>	<b>2</b>
<b>2.0 THEORETICAL CONSIDERATION.....</b>	<b>3</b>
<b>2.1 DIFFERENCE BETWEEN BULK WAVES AND SURFACE WAVES.....</b>	<b>3</b>
<b>2.1.1 Longitudinal wave .....</b>	<b>4</b>
<b>2.1.2 Transverse wave .....</b>	<b>4</b>
<b>2.1.3 Rayleigh wave .....</b>	<b>5</b>
<b>2.2 ELASTIC CONSTANTS AND SURFACE WAVE .....</b>	<b>7</b>
<b>2.2.1 Propagation at an interface between isotropic solid and liquid .....</b>	<b>7</b>
<b>2.2.2 Elastic constants.....</b>	<b>11</b>
<b>2.2.3 Acoustic waves in solids .....</b>	<b>16</b>
<b>2.2.4 Ratio of the velocity of Rayleigh wave and transverse wave .....</b>	<b>21</b>
<b>2.3 RESEARCH HISTORY.....</b>	<b>22</b>
<b>2.4 PRINCIPLE OF MEASUREMENT.....</b>	<b>23</b>
<b>2.4.1 Snell's Law and critical angle.....</b>	<b>23</b>
<b>2.4.2 Time-resolved Defocusing Method.....</b>	<b>25</b>

2.4.3	Chemical Corrosion.....	27
3.0	EXPERIMENTAL PROCEDURE.....	30
3.1	EQUIPMENT SET-UP .....	30
3.2	PREPARATION OF SAMPLES .....	31
3.3	MEASUREMENT OF THE DENSITY .....	33
3.4	DATA RECORDING DURING TIME-RESOLVED DEFOCUSING .....	34
4.0	DATA PROCESSING AND RESULTS .....	37
4.1	RESULTS OF THE STANDARD SAMPLE .....	37
4.2	RESULTS OF THE ADDITIVE MANUFACTURED SAMPLE.....	39
5.0	DISCUSSION AND CONCLUSION .....	41
6.0	EXPERIMENT IMPROVEMENT AND FUTURE WORK.....	42
6.1	THE VULNERABLE STEEL TYPE .....	42
6.2	THE PATTERNS OF CORROSION .....	42
6.3	THE PORTABILITY OF THE LINE-FOCUSED TRANSDUCER SYSTEM.....	43
	APPENDIX A .....	44
	APPENDIX B .....	47
	BIBLIOGRAPHY.....	50

## LIST OF TABLES

Table 1. Parameters and Elastic Properties' Calculation of Standard Samples .....	38
Table 2. Stainless Steel Grade 420 Typical Material Properties .....	39
Table 3. Parameters and Elastic Properties' Calculation of Additive Manufactured Samples.....	40

## LIST OF FIGURES

Figure 1. Particles displacement of the longitudinal wave .....	4
Figure 2. Particles displacement of the transverse wave .....	5
Figure 3. Particles displacement of the Rayleigh wave .....	6
Figure 4. Coordinate definition at a two half-space boundary.....	7
Figure 5. Deformation of a cubic element .....	14
Figure 6. A pair of normal stress illustration of a cubic element.....	16
Figure 7. A pair of shear stress illustration of a cubic element.....	17
Figure 8. The wave's refraction .....	24
Figure 9. Working principle of concave transducer [16] .....	26
Figure 10. Electrochemical Corrosion in Active Metal [17] .....	28
Figure 11. Schematic diagram of the Ultrasonic Testing System.....	31
Figure 12. Samples before corrosion .....	32
Figure 13. Samples after corrosion .....	32
Figure 14. The process of the corrosion.....	32
Figure 15. Measurement of the sample's volume by drainage method .....	33
Figure 16. Waveform at the focal position .....	34
Figure 17. Waveform during the defocus process .....	36

Figure 18. Defocus-length with respect to traveling time of standard samples .....	37
Figure 19. Defocus-length with respect to traveling time of additive manufactured samples .....	40
Figure 20. Code for solving intersection problem .....	48
Figure 21. Plot for solving the eq. (B-1).....	48

## NOMENCLATURE

$\lambda$	Wave Length
$\omega$	Angular Frequency
$k$	Wave Number
$\rho$	Density
$\sigma$	Stress
$\epsilon$	Strain
$c$	Elastic Constant
$s$	Elastic Constant in Reverse
$B$	Bulk Modulus
$V$	Volume
$E$	Young's Modulus (Elastic Modulus)
$\nu$	Poisson's Ratio
$F$	Applied Force
$T$	Period
$f$	Focal Distance
$z$	Defocused Position
$v_w$	Propagating Velocity in Water
$v_l$	Velocity of Longitudinal Wave

- $v_t$  Velocity of Transverse Wave
- $v_R$  Velocity of Rayleigh Wave
- $\theta_i$  Angle of Incidence
- $\theta_r$  Angle of Refraction
- $\theta_R$  Second Critical Angle (Rayleigh Angle)
- $v_i$  Velocity of Incidence
- $v_r$  Velocity of Refraction

## ACKNOWLEDGEMENT

This research has benefited from interactions with many people over this year. I would like to offer my kindest regards to them.

In the first place, I would like to thank my advisor, Dr. Qing-Ming Wang, not only for his advice in conducting experiment but also for his thought-provoking guidance in my career development. In the meanwhile, I appreciate my committee members: Dr. William Slaughter and Dr. Patrick Smolinski, for their time and expertise to enrich my work.

Secondly, this thesis would not be completed without the help from my research group members: Qiuyan Li and Yuxiang Wang. They offer some previous experience to help me faster enter this research and avoid some potential failures. Furthermore, I want to give my thanks to a friend met on IUS 2017, Nutthawut Suchato, for his help in expanding my horizon of this research field.

There are too many to list one by one here. Most of all, I am especially thankful to my parents for their steadfast support and encouragement.

## **1.0 INTRODUCTION**

In the recent decades, additive manufacturing represented by 3-D printing industry has swept across the world. It makes the metalworking no longer be restricted to conventional processing and manufacturing methods (e.g., casting, forging, *etc.*) and gives more imagination to modern fabrication. During the fabrication, most metallic additive manufactured alloys experience repeated solid-state phase transformations, which gives them some unparalleled properties that conventional fabricated parts can never have [1].

Nevertheless, corrosion exists obstinately for all metal alloys no matter they are manufactured by traditional subtractive means or by additive manufacturing methods. The failure to monitor the seriousness of corrosion can cause a catastrophic accident. Compared with other Non-Destructive Testing methods, the method of ultrasonic surface wave testing has a lot of advantages including portability, efficiency, and un-contamination *etc.* [2]. This makes it a quite promising method to evaluate or monitor electrochemical corrosion, which is generally initiated at the surface of metal alloys in practical applications.

### **1.1 CURRENT VESSEL CORROSION TEST METHOD**

One of the most widely used corrosion evaluating area is ship hulls' corrosion monitoring. In-service continuous ultrasonic thickness monitoring of ship hulls, conducted in the pulse-echo

mode from inside the ships, has the potential to reduce maintenance and service costs. This technique can also help to mitigate significant inaccuracy in estimating wall thickness associated with surface corrosion while the ship is in service [3].

However, the ultrasonic transducer operating in this method is through the pulse echo mode, which works like a sonar. It can only detect the variation of the vessel hulls' thickness by launching and receiving the echoes. By observing the reflected echo waves on the oscilloscope, the thickness change can be calculated so that the corrosion degree will be estimated. In this method, the corrosion degree is evaluated through only one dimension – thickness, which is not accurate enough to assess the corrosion of a vessel.

## **1.2 MOTIVATION**

To improve and expand the methods for the evaluation of the corrosion, we propose to apply the surface Rayleigh wave onto the corrosion degree evaluation to replace merely using the echo mode. Furthermore, the application of surface Rayleigh wave in corrosion evaluation can not only provide the information of the thickness of the ship hulls but also some other information that could be dug behind these datum, such as the variation of the elastic properties. With more dimension in assessing the corrosion degree of the hulls, it is possible to use this technique in wider practical field. For example, by providing the corrosion evaluation and elastic properties of the vessel hulls, it can be used in helping choose a salvage scheme and make a decision in sunken vessel salvage.

## **2.0 THEORETICAL CONSIDERATION**

As mentioned in the previous section, most of the current vessel corrosion test methods rely on the echoes propagating between the interfaces of the sample to be tested, which can only provide the information about the thickness variation. To improve the corrosion measurement and monitoring, we consider using the surface acoustic waves to obtain more information, such as the elastic properties, to evaluate the degree of the corrosion without destroying the specimen.

### **2.1 DIFFERENCE BETWEEN BULK WAVES AND SURFACE WAVES**

In physics, a wave is an oscillation accompanied by a transfer of energy. Mechanical waves are waves which propagate through a material medium, e.g. solid, liquid and gas, at some speed which depends on the elastic and inertial properties of that medium.[4] Different wave has different oscillation resulting from its unique particles' movement. In general, bulk waves are elastic waves propagating in solids. They are categorized into a longitudinal wave (or primary wave), and a transverse wave (or shear wave); surface waves include Rayleigh wave, Love wave, Lamb wave and *etc.* Since the Rayleigh wave was the wave we chose to observe in this study, let us put emphasis on the principle of the Rayleigh wave and the comparison between the Rayleigh wave and other bulk waves in the following article.

### 2.1.1 Longitudinal wave

From the illustration of the longitudinal wave's propagation as shown in figure below, we can see that each particle oscillates back and forth around its equilibrium position at its own pace so that they shape the compression or rarefaction area together. After changing the status of between the compression and rarefaction in turns, the wave's propagation in a specific direction will be formed. It is worth to notice that in this period, the particles do not spread with the propagation of the wave. It seems like the particles transit accompanied by the wave motion. However, these particles only pass the energy along the propagation of the wave as a medium.

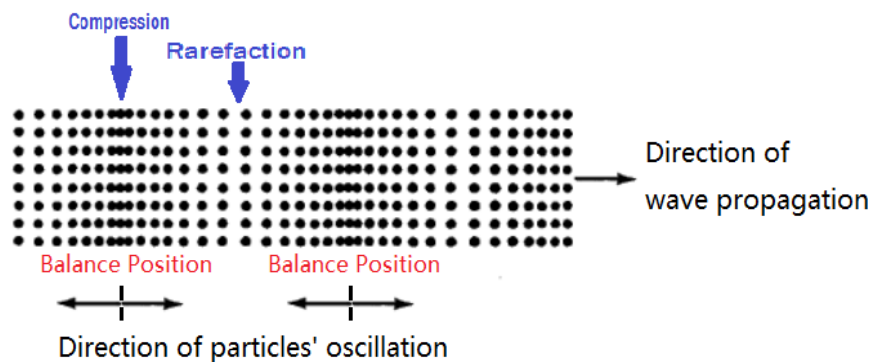


**Figure 1.** Particles displacement of the longitudinal wave

In a word, a traveling wave that causes the particles to oscillate in the direction in parallel with the propagation of the wave is called a longitudinal wave. The distance between two contiguous compressions (or rarefaction) equals a wavelength –  $\lambda$ .

### 2.1.2 Transverse wave

Compared to the longitudinal wave, the particles' movement in transverse wave has some common places. For example, the oscillation of each particle also has an equilibrium position;

and the particles do not move along with the wave either. A significant difference is that the particle moves perpendicular to the propagation of the wave. In the figure shown below, we can see that the particles oscillate in vertical direction up and down around its original position while the wave moves in horizontal direction. Another difference distinguished from the longitudinal wave is that transverse wave does not present any compression or rarefaction area. It has crests and troughs instead.

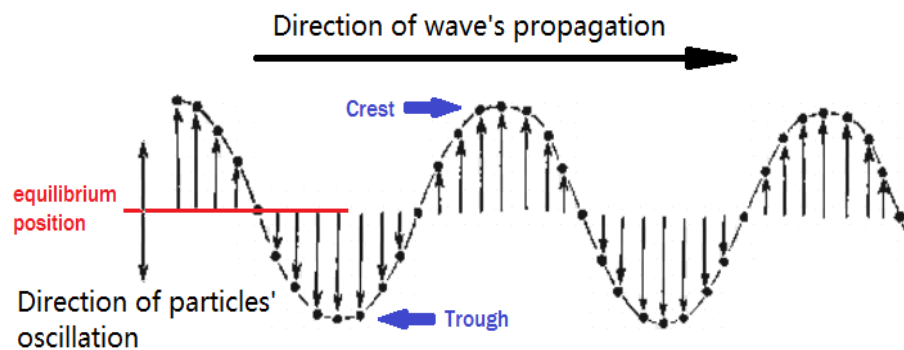


**Figure 2.** Particles displacement of the transverse wave

To summarize, a traveling wave that causes the particles of the medium to oscillate in the direction orthogonal to the wave motion is called a transverse wave or shear wave. The distance between two contiguous crests (or troughs) equals a wavelength.

### 2.1.3 Rayleigh wave

As the longitudinal wave and the transverse wave mentioned before, the particles' displacement of the Rayleigh wave can be treated as a combination of both longitudinal and transverse motions in some degree. Let us imagine that an individual particle of the medium in Rayleigh wave has to oscillate not only in vertical direction but also in horizontal direction,

which means it can be perturbed back and forth while it vibrates up and down. Thus, the net motion of each individual particle is like an ellipse as show in the following figure.

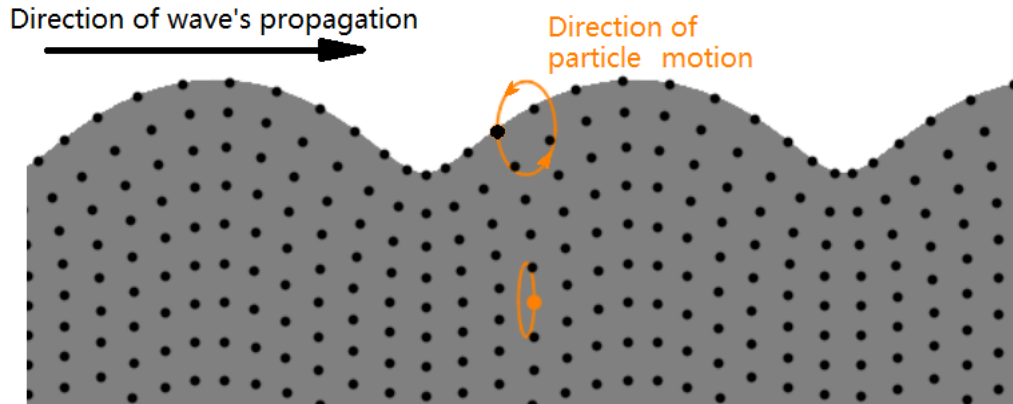


**Figure 3.** Particles displacement of the Rayleigh wave

From the late 19<sup>th</sup> century, the waves that can be propagated over the plane boundary between an elastic half-space and a sufficiently rarefied medium are named after the English scientist Lord Rayleigh (J. Strutt) to memorize his historical contribution. The Rayleigh waves involved the principal type of earthquake wave observed at that time in earth tremors. [5] As we can see in the above figure, the motion of the particles near the surface is severer than it beneath the surface, which can be told from the sizes of the oval motion trails. The maximum energy of a surface wave, therefore, is concentrated on the surface where the waves are generated. Compared with other types of earthquake waves, such as primary wave (longitudinal wave) and secondary wave (transverse wave), the destructiveness of the surface wave is tremendous. That is the reason why the surface waves have been studied deeply and widely in seismology.

Besides researches in the seismology field, the Rayleigh surface wave in the ultrasonic range has found considerable application. Since it is sensitive to the surficial condition, it can be used to detect the state of the surface layer of a sample, i.e., in the inspection of surface and near-surface defects in materials, such as metals, alloys, glasses etc. In this study, we consider how to

use some characters of the Rayleigh wave to derive the relationship between the material's elastic properties and the propagation velocities instead of using the Rayleigh wave to inspect the flaws of the material directly.

## 2.2 ELASTIC CONSTANTS AND SURFACE WAVE

### 2.2.1 Propagation at an interface between isotropic solid and liquid

Let us consider the propagation of surface waves at the boundary between two half-space – a solid and a liquid. As shown in the figure below, the direction of the wave motion is coincident with the x-axis.

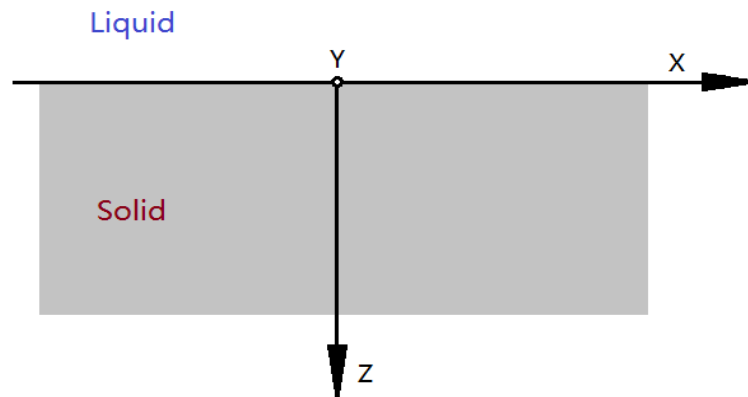


Figure 4. Coordinate definition at a two half-space boundary

We denote the potentials of the longitudinal and transverse wave by  $\varphi$  and  $\psi$  respectively. It must satisfy the following wave equations:

$$\frac{\partial^2 \varphi}{\partial x^2} + \frac{\partial^2 \varphi}{\partial z^2} + k_t^2 \varphi = 0 \quad (2.2.1-1)$$

$$\frac{\partial^2 \psi}{\partial x^2} + \frac{\partial^2 \psi}{\partial z^2} + k_t^2 \psi = 0 \quad (2.2.1-2)$$

In these two expressions,  $k_l = \omega\sqrt{\rho/(\lambda + 2\mu)}$  and  $k_t = \omega\sqrt{\rho/\mu}$  are the wave numbers for longitudinal and transverse modes respectively, where  $\omega$  is the circular frequency,  $\lambda$  and  $\mu$  are the elastic Lamè constants, and  $\rho$  is the density of the medium. [6]

In the meantime, the expression for the potential  $\varphi_{Lq}$  in the liquid must satisfy the analogous equation as following:

$$\frac{\partial^2 \varphi_{Lq}}{\partial x^2} + \frac{\partial^2 \varphi_{Lq}}{\partial z^2} + k_{Lq}^2 \varphi_{Lq} = 0 \quad (2.2.1-3)$$

Similar to previous wave equations,  $k_{Lq}$  also represents the wave numbers in the liquid, which equals  $\omega/c_{Lq}$ , where  $c_{Lq}$  is the velocity in the liquid. We only need to consider the longitudinal situation here, since there is no shear modulus in the state of liquid.

Let us denote the components of the particle displacement along the x and z-axes by  $U$  and  $W$  respectively, that can be written in terms of  $\varphi$  and  $\psi$  as the following equations:

$$U = \frac{\partial \varphi}{\partial x} - \frac{\partial \psi}{\partial z} \quad (2.2.1-4)$$

$$W = \frac{\partial \varphi}{\partial z} + \frac{\partial \psi}{\partial x} \quad (2.2.1-5)$$

Then the stress components may also be represented in terms of  $\varphi$  and  $\psi$  according to the equations:

$$\sigma_{xx} = \lambda \left( \frac{\partial^2 \varphi}{\partial x^2} + \frac{\partial^2 \varphi}{\partial z^2} \right) + 2\mu \left( \frac{\partial^2 \varphi}{\partial x^2} - \frac{\partial^2 \psi}{\partial x \partial z} \right) \quad (2.2.1-6)$$

$$\sigma_{zz} = \lambda \left( \frac{\partial^2 \varphi}{\partial x^2} + \frac{\partial^2 \varphi}{\partial z^2} \right) + 2\mu \left( \frac{\partial^2 \varphi}{\partial z^2} + \frac{\partial^2 \psi}{\partial x \partial z} \right) \quad (2.2.1-7)$$

$$\sigma_{xz} = \mu \left( \frac{\partial U}{\partial z} + \frac{\partial W}{\partial x} \right) = \mu \left( 2 \frac{\partial^2 \varphi}{\partial x \partial z} - \frac{\partial^2 \psi}{\partial z^2} + \frac{\partial^2 \psi}{\partial x^2} \right) \quad (2.2.1-8)$$

Due to a plane harmonic wave propagating in the positive x-direction, we can assume that the potential  $\varphi$  and  $\psi$  have forms like these:

$$\varphi = F(z)e^{i(kx-\omega t)} \quad (2.2.1-9)$$

$$\psi = G(z)e^{i(kx-\omega t)} \quad (2.2.1-10)$$

Where  $k$  is the surface wave number, and  $\omega$  is the circular frequency.

Substituting them into eq. (2.2.1-1) & eq. (2.2.1-2), we can have:

$$\frac{d^2F(z)}{dz^2} - (k^2 - k_t^2)F(z) = 0 \quad (2.2.1-11)$$

$$\frac{d^2G(z)}{dz^2} - (k^2 - k_t^2)G(z) = 0 \quad (2.2.1-12)$$

By eliminating  $e^{i(kx-\omega t)}$  from both sides of each equation.

Obviously, these two homogeneous-linear differential equations have two linearly independent solutions:

$$F(z) = \pm A e^{-\left(\sqrt{k^2 - k_t^2}\right) \cdot z} \quad (2.2.1-13)$$

$$G(z) = \pm B e^{-\left(\sqrt{k^2 - k_t^2}\right) \cdot z} \quad (2.2.1-14)$$

Where  $A$  and  $B$  are arbitrary constants. Here, negative powers were chosen because as the depth  $z$  increased, the potentials were expected to exhibit corresponding exponential decay.

So far, our assumed expression of  $\varphi$  and  $\psi$  should be:

$$\varphi = A e^{-\alpha \cdot z} e^{i(kx-\omega t)} \quad (2.2.1-15)$$

$$\psi = B e^{-\beta \cdot z} e^{i(kx-\omega t)} \quad (2.2.1-16)$$

Where  $\alpha^2 = k^2 - k_t^2$  and  $\beta^2 = k^2 - k_t^2$

Since we seek a surface wave solution, the potentials  $\varphi$  and  $\psi$  in the solid must describe longitudinal and transverse inhomogeneous waves propagating in the  $x$  direction and decaying in the  $z$  direction. The conditions of the problem demand that the stresses  $\sigma_{zz}$  and  $\sigma_{xz}$  go to zero at the position  $z = 0$ . As a result, we finally obtain the expression for  $\varphi$  and  $\psi$ :

$$\varphi = Ae^{i(kx-\omega t)-\alpha z} \quad (2.2.1-17)$$

$$\psi = -iA \frac{2k\alpha}{k^2+\beta^2} e^{i(kx-\omega t)-\beta z} \quad (2.2.1-18)$$

Then the particle displacement along x- and z- axes of solid part can be written by substituting  $\varphi$  and  $\psi$  expressions into eq. (2.2.1-4) & eq. (2.2.1-5):

$$U = Ak \left( e^{-\alpha z} - \frac{2\alpha\beta}{k^2+\beta^2} e^{-\beta z} \right) e^{i(kx-\omega t+\frac{\pi}{2})} \quad (2.2.1-19)$$

$$W = -A\alpha \left( e^{-\alpha z} - \frac{2k^2}{k^2+\beta^2} e^{-\beta z} \right) e^{i(kx-\omega t)} \quad (2.2.1-20)$$

Now let us consider the wave propagating in the liquid. It must pursue a path along the x-axis with a velocity equal to the phase velocity of the aforementioned inhomogeneous waves. This means that the wave in the liquid has to satisfy the boundary condition as it in the solid, the longitudinal stress in the liquid and solid should be identical, and the tangential stress should be zero.

In a similar way, we are able to obtain the components of the displacements along the x- and z- axes in the liquid:

$$U_{Lq} = -Ak \frac{\alpha k_t^2}{\sqrt{k_{Lq}^2 - k^2}(k^2 + \beta^2)} e^{i[kx - \omega t - (\sqrt{k_{Lq}^2 - k^2}) \cdot z]} \quad (2.2.1-21)$$

$$W_{Lq} = Ak_t \frac{\alpha k_t}{(k^2 + \beta^2)} e^{i[kx - \omega t - (\sqrt{k_{Lq}^2 - k^2}) \cdot z]} \quad (2.2.1-22)$$

Again,  $k$  is the surface wave number, and  $A$  is an arbitrary constant. The characteristic equation determining the wave number  $k$  has the form: [6]

$$4k^2\alpha\beta - (k^2 + \beta^2)^2 - i \frac{\rho_{Lq}}{\rho} \cdot \frac{\alpha k_t^4}{\gamma} = 0 \quad (2.2.1-23)$$

Where  $\alpha = \sqrt{k^2 - k_t^2}$ ,  $\beta = \sqrt{k^2 - k_t^2}$ , and  $\gamma = \sqrt{k_{Lq}^2 - k^2}$ .

### 2.2.2 Elastic Constants

As we know, the Hooke's Law can be written as  $\sigma = c\varepsilon$ , where  $c$  is an elastic constant. In a solid, the deformation caused by the wave propagation is very small. Therefore, we can treat the internal stresses and strains have a linear relationship as described in Hooke's Law. A generalized form is:

$$\sigma_{ij} = \sum_{kl} c_{ijkl} \varepsilon_{kl} \quad (2.2.2-1)$$

The subscripts  $ijkl$  count from 1 through 3 to represent the orthogonal axes' direction in a three-dimensional space. And the coefficients  $c_{ijkl}$  are components of the stiffness tensor. According to the knowledge of permutation and combination, we can easily figure out that there are  $3^4 = 81$  of the coefficients  $c_{ijkl}$ . Fortunately, the tensors  $\sigma_{ij}$  and  $\varepsilon_{kl}$  are symmetric, the coefficient makes no difference if the first two or last two subscripts are interchanged. That means:  $c_{ijkl} = c_{jikl}$  and  $c_{ijkl} = c_{ijlk}$ . Due to this benefit, the number of the elastic coefficients reduce from 81 to 36. Indeed, a pair of unordered indices ( $i, j$ ) can give only six independent values.

Thus, we are able to denote them in a different way called Voigt Notation<sup>1</sup>. Let us take a look at the elastic constant matrix:

$$\begin{pmatrix} c_{11} & c_{12} & c_{13} & c_{14} & c_{15} & c_{16} \\ c_{21} & c_{22} & c_{23} & c_{24} & c_{25} & c_{26} \\ c_{31} & c_{32} & c_{33} & c_{34} & c_{35} & c_{36} \\ c_{41} & c_{42} & c_{43} & c_{44} & c_{45} & c_{46} \\ c_{51} & c_{52} & c_{53} & c_{54} & c_{55} & c_{56} \\ c_{61} & c_{62} & c_{63} & c_{64} & c_{65} & c_{66} \end{pmatrix} \quad (2.2.2-2)$$

---

<sup>1</sup> For details, see the Appendix A

According to symmetry,  $c_{12} = c_{21}$ , *etc.*, we can reduce the independent coefficients from 36 to 21. This matrix is called TRICLINIC in crystals of the triclinic system, and it is the lowest symmetry crystal.

For the ORTHORHOMBIC crystal, there are three mutually perpendicular two-fold rotation axes and three mutually perpendicular mirror planes. Let us image that  $x_1$ ,  $x_2$  and  $x_3$  are coincident with those three two-fold rotation axes. This means that any  $c_{ijkl}$  for which any subscript, 1, 2, or 3, appears an odd number of times must be zero. [8] Applying this condition systematically to the  $c_{ijkl}$  leads to the orthorhombic elastic constant matrix as follow:

$$\begin{pmatrix} c_{11} & c_{12} & c_{13} & 0 & 0 & 0 \\ c_{21} & c_{22} & c_{23} & 0 & 0 & 0 \\ c_{31} & c_{32} & c_{33} & 0 & 0 & 0 \\ 0 & 0 & 0 & c_{44} & 0 & 0 \\ 0 & 0 & 0 & 0 & c_{55} & 0 \\ 0 & 0 & 0 & 0 & 0 & c_{66} \end{pmatrix} \quad (2.2.2-3)$$

Now the independent coefficients reduce to 9. Based on this principle, we can easily derive the CUBIC crystal's elastic constant matrix from orthorhombic one by noting that the  $x_i$  axes are all equivalent for cubic symmetry. Thus,  $c_{12} = c_{1122} = c_{1133} = c_{13}$ , *etc.*

$$\begin{pmatrix} c_{11} & c_{12} & c_{12} & 0 & 0 & 0 \\ c_{12} & c_{11} & c_{12} & 0 & 0 & 0 \\ c_{12} & c_{12} & c_{11} & 0 & 0 & 0 \\ 0 & 0 & 0 & c_{44} & 0 & 0 \\ 0 & 0 & 0 & 0 & c_{44} & 0 \\ 0 & 0 & 0 & 0 & 0 & c_{44} \end{pmatrix} \quad (2.2.2-4)$$

So far, we have 3 independent elastic constants in cubic symmetry element. Obviously, an isotropic material has all of these symmetry characters as mentioned before. Therefore, it has these three elastic constants -  $c_{11}$ ,  $c_{12}$ ,  $c_{44}$  at least. Furthermore, if we rotate the cubic  $c_{1111}$  about the  $x_3$  axis by an arbitrary angle  $\theta$ , we can obtain a relationship between these three elastic constants. The four-rank tensor transformation formula is given by [9]:

$$c'_{ijkl} = \sum_{mnop} a_{im} a_{jn} a_{ko} a_{lp} c_{mnop} \quad (2.2.2-5)$$

Where  $a_{im}$  is a direction cosine where the first subscript refers to the  $x'_i$  axis while the second refers to the  $x_m$  axis. This transformation rule gives:

$$c_{1111} \rightarrow c_{1111}(\cos^4 \theta + \sin^4 \theta) + 2c_{1122} \cos^2 \theta \sin^2 \theta + 4c_{2323} \cos^2 \theta \sin^2 \theta \quad (2.2.2-6)$$

Requiring the right-hand side of expression (2.2.2-6) to equal  $c_{1111}$  and apply the Voigt Notation gives:

$$c_{11} = c_{11}(\cos^4 \theta + \sin^4 \theta) + 2c_{12} \cos^2 \theta \sin^2 \theta + 4c_{44} \cos^2 \theta \sin^2 \theta$$

$$4c_{44} = \left( \frac{\cos^2 \theta + \sin^2 \theta - \cos^4 \theta - \sin^4 \theta}{\cos^2 \theta \sin^2 \theta} \right) c_{11} - 2c_{12}$$

$$4c_{44} = \left( \frac{1}{\sin^2 \theta} - \frac{\cos^2 \theta}{\sin^2 \theta} + \frac{1}{\cos^2 \theta} - \frac{\sin^2 \theta}{\cos^2 \theta} \right) c_{11} - 2c_{12}$$

$$c_{44} = \frac{1}{2}(c_{11} - c_{12}) \quad (2.2.2-7)$$

To express the elastic parameters in terms of the elastic constants  $c_{mn}$ , one of these elastic parameters called *Bulk Modulus* will be addressed at first. Let us take a look at an infinitesimal cube in the solid as shown below. The length of each side equals  $a$ . After the stresses are applied at each face, the elongations along each axis are  $\Delta x$ ,  $\Delta y$ , and  $\Delta z$ , respectively. Thus, the volume of this cube after deformation is  $\Delta V = \Delta x \cdot \Delta y \cdot \Delta z$ . Since the deformation is very tiny, we can assume that the volume change is:

$$\frac{\Delta V}{V} \approx \frac{\Delta x}{a} + \frac{\Delta y}{a} + \frac{\Delta z}{a} = \varepsilon_1 + \varepsilon_2 + \varepsilon_3 \quad (2.2.2-8)$$

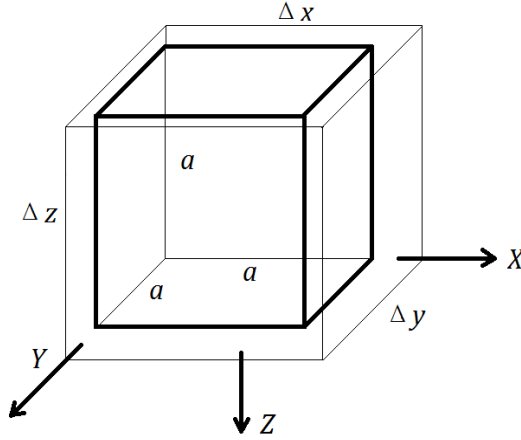


**Figure 5.** Deformation of a cubic element

Recalling from the eq. (B-9), we can derive a compliance matrix which is similar to the elastic constant matrix:

$$\begin{pmatrix} \varepsilon_1 \\ \varepsilon_2 \\ \varepsilon_3 \\ \varepsilon_4 \\ \varepsilon_5 \\ \varepsilon_6 \end{pmatrix} = \begin{pmatrix} S_{11} & S_{12} & S_{13} & S_{14} & S_{15} & S_{16} \\ S_{21} & S_{22} & S_{23} & S_{24} & S_{25} & S_{26} \\ S_{31} & S_{32} & S_{33} & S_{34} & S_{35} & S_{36} \\ S_{41} & S_{42} & S_{43} & S_{44} & S_{45} & S_{46} \\ S_{51} & S_{52} & S_{53} & S_{54} & S_{55} & S_{56} \\ S_{61} & S_{62} & S_{63} & S_{64} & S_{65} & S_{66} \end{pmatrix} \begin{pmatrix} \sigma_1 \\ \sigma_2 \\ \sigma_3 \\ \sigma_4 \\ \sigma_5 \\ \sigma_6 \end{pmatrix} \quad (2.2.2-9)$$

Besides, the definition of the bulk modulus is

$$B = -V \frac{dP}{dV} \cong -\frac{\Delta P}{\Delta V/V} \quad (2.2.2-10)$$

Solving these three equations simultaneously with the hydrostatic conditions:  $\sigma_1 = \sigma_2 = \sigma_3 = -\Delta P$ , and  $\sigma_4 = \sigma_5 = \sigma_6 = 0$ .

$$\begin{cases} \varepsilon_1 = -\Delta P(s_{11} + s_{12} + s_{13}) \\ \varepsilon_2 = -\Delta P(s_{12} + s_{22} + s_{23}) \\ \varepsilon_3 = -\Delta P(s_{13} + s_{23} + s_{33}) \end{cases}$$

$$\therefore B = \frac{1}{s_{11} + s_{22} + s_{33} + 2(s_{12} + s_{23} + s_{13})} \quad (2.2.2-11)$$

According to the cubic symmetry, we have  $s_{11} = s_{22} = s_{33}$  and  $s_{12} = s_{23} = s_{13}$ . Hence, the bulk modulus becomes:

$$B_{cubic} = \frac{1}{3(s_{11}+2s_{12})} \quad (2.2.2-12)$$

From the cubic elastic constant matrix, we can easily write the following equations:

$$\begin{cases} \sigma_1 = c_{11}\varepsilon_1 + c_{12}(\varepsilon_2 + \varepsilon_3) \\ \sigma_2 = c_{11}\varepsilon_2 + c_{12}(\varepsilon_3 + \varepsilon_1) \\ \sigma_3 = c_{11}\varepsilon_3 + c_{12}(\varepsilon_1 + \varepsilon_2) \end{cases} \quad \text{and} \quad \begin{cases} \sigma_4 = c_{44}\varepsilon_4 \\ \sigma_5 = c_{44}\varepsilon_5 \\ \sigma_6 = c_{44}\varepsilon_6 \end{cases}$$

For the previous equation set, combining the second and third equations, we can obtain:

$$\sigma_2 + \sigma_3 = c_{11}(\varepsilon_2 + \varepsilon_3) + c_{12}(2\varepsilon_1 + \varepsilon_2 + \varepsilon_3) \quad (2.2.2-13)$$

Solve with the first equation by eliminating the " $\varepsilon_2 + \varepsilon_3$ " term, we have:

$$(c_{11}^2 + c_{11}c_{12} - 2c_{12}^2)\varepsilon_1 = (c_{11} + c_{12})\sigma_1 - c_{12}\sigma_2 - c_{12}\sigma_3 \quad (2.2.2-14)$$

In the similar way, we can express  $\varepsilon_2$  and  $\varepsilon_3$  in terms of  $c_{11}$ ,  $c_{12}$ ,  $\sigma_1$ ,  $\sigma_2$ , and  $\sigma_3$ .

Thus, we express the strains in terms of the stresses, and get the cubic compliance matrix in terms of the elastic constants:

$$\begin{pmatrix} \varepsilon_1 \\ \varepsilon_2 \\ \varepsilon_3 \\ \varepsilon_4 \\ \varepsilon_5 \\ \varepsilon_6 \end{pmatrix} = \begin{pmatrix} \frac{c_{11}+c_{12}}{N} & -\frac{c_{12}}{N} & -\frac{c_{12}}{N} & 0 & 0 & 0 \\ -\frac{c_{12}}{N} & \frac{c_{11}+c_{12}}{N} & -\frac{c_{12}}{N} & 0 & 0 & 0 \\ -\frac{c_{12}}{N} & -\frac{c_{12}}{N} & \frac{c_{11}+c_{12}}{N} & 0 & 0 & 0 \\ 0 & 0 & 0 & 1/c_{44} & 0 & 0 \\ 0 & 0 & 0 & 0 & 1/c_{44} & 0 \\ 0 & 0 & 0 & 0 & 0 & 1/c_{44} \end{pmatrix} \begin{pmatrix} \sigma_1 \\ \sigma_2 \\ \sigma_3 \\ \sigma_4 \\ \sigma_5 \\ \sigma_6 \end{pmatrix} \quad (2.2.2-15)$$

Where  $N = c_{11}^2 + c_{11}c_{12} - 2c_{12}^2$ .

Then  $B_{cubic}$  can be written in terms of the elastic constants

$$B_{cubic} = \frac{c_{11}+2c_{12}}{3} \quad (2.2.2-16)$$

And Young's modulus can also be expressed in terms of the elastic constants:

$$E_1 = \frac{1}{s_1} = \frac{c_{11}^2+c_{11}c_{12}-2c_{12}^2}{c_{11}+c_{12}} \quad (2.2.2-17)$$

The index 1 indicates that this Young's modulus represents the linear relationship between the tensile stress and the corresponding strain along the  $x_1$  axis. The same results can be derived for the other two directions because of the cubic symmetry.

Recalling for the eq. (2.2.2-7), we can easily obtain the Young's modulus for the isotropic material in terms of the elastic constants by applying the relation  $c_{12} = c_{11} - 2c_{44}$  :

$$E = \frac{3c_{11}c_{44} - 4c_{44}^2}{c_{11} - c_{44}} \quad (2.2.2-18)$$

### 2.2.3 Acoustic waves in solids

Now let us take a look at an infinitesimal cube in the solid as shown below.

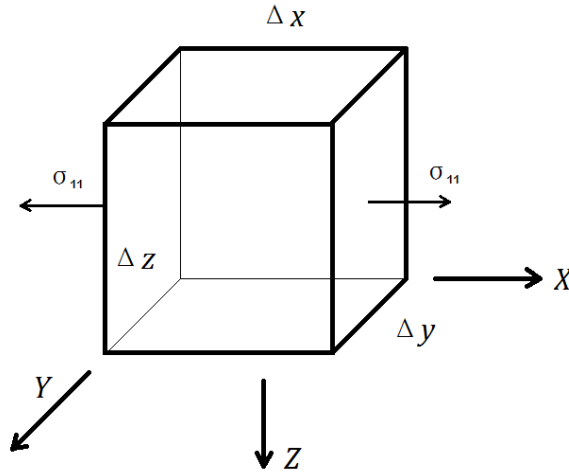


**Figure 6.** A pair of normal stress illustration of a cubic element

The force applied in x-direction should be equal to:

$$F_{x_{11}} = \sigma_{11} \cdot \Delta y \Delta z = \left( \frac{\partial \sigma_{11}}{\partial x} \Delta x \right) \Delta y \Delta z \quad (2.2.3-1)$$

In the similar way, we can obtain the relationship between the force and the shear stress in the same direction. One pair of shear stress  $\sigma_{12}$  is illustrated in the figure shown below. It is

worthy to notice that the shear stress  $\sigma_{ij}$  is the stress which is applied at  $j$  face (the plane which is perpendicular to the  $j$  axis, here we use 1,2,3 to represent the  $x, y, z$ , respectively, to better match the notation mentioned in the previous sections) pointing to  $i$  direction.

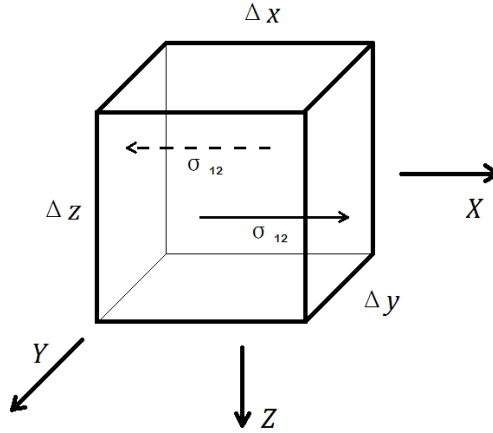


**Figure 7.** A pair of shear stress illustration of a cubic element

Reference to Figure 7 shows

$$F_{x_{12}} = \sigma_{12} \cdot \Delta x \Delta z = \left( \frac{\partial \sigma_{12}}{\partial y} \Delta y \right) \Delta x \Delta z \quad (2.2.3-2)$$

Similarly, we can have

$$F_{x_{13}} = \sigma_{13} \cdot \Delta x \Delta y = \left( \frac{\partial \sigma_{13}}{\partial z} \Delta z \right) \Delta x \Delta y \quad (2.2.3-3)$$

Apply the Newton's Second Law and summarize these three equations together, we can get the net force acting to x-direction:

$$F_x = m a_x$$

$$\left( \frac{\partial \sigma_{11}}{\partial x} + \frac{\partial \sigma_{12}}{\partial y} + \frac{\partial \sigma_{13}}{\partial z} \right) \Delta x \Delta y \Delta z = \rho \Delta V \cdot \frac{\partial^2 u_1}{\partial t^2}$$

$$\left( \frac{\partial \sigma_{11}}{\partial x} + \frac{\partial \sigma_{12}}{\partial y} + \frac{\partial \sigma_{13}}{\partial z} \right) = \rho \frac{\partial^2 u_1}{\partial t^2} \quad (2.2.3-4)$$

Eq. (2.2.3-4) is obtained by eliminating  $\Delta V = \Delta x \Delta y \Delta z$  from both sides of the equation;  $u_1$  is the deformation of the cube in x direction.

Consequently, we can rewrite the Eq. (2.2.3-4) in a general form:

$$\sum_j^3 \frac{\partial \sigma_{ij}}{\partial x_i} = \rho \frac{\partial^2 u_i}{\partial t^2} \quad (2.2.3-5)$$

In the meanwhile,  $i$  runs from 1 to 3 to represent the  $x, y,$  and  $z$  axis respectively.

Recall the eq. (2.2.2-1) and make an exchange of virtual subscripts within a sum produces,

$$\sum_j \frac{\partial \sigma_{ij}}{\partial x_i} = \sum_{jkl} c_{ijkl} \frac{\partial^2 u_k}{\partial x_j \partial x_l} \quad (2.2.3-6)$$

Then we have

$$\sum_{jkl} c_{ijkl} \frac{\partial^2 u_k}{\partial x_j \partial x_l} = \rho \frac{\partial^2 u_i}{\partial t^2} \quad (2.2.3-7)$$

Similar to Eq. (2.2.1-9), let us assume the plane wave solution is:

$$u_i = u_i^0 e^{i(\vec{K} \cdot \vec{r} - \omega t)} \quad (2.2.3-8)$$

Where  $\vec{K}$  is the wave vector ( $|\vec{K}| = K = 2\pi/\lambda$ , with  $K$  being the wave numbers and  $\lambda$  being the wave length towards the  $\vec{K}$  direction),  $\omega$  is the angular frequency, and the index  $i$  ranges from 1 to 3 to represent the three directions. Note that  $\vec{K} \cdot \vec{r} = \sum_l K_l x_l$ . We can obtain the following expression by substituting the eq. (2.2.3-8) into the eq. (2.2.3-7) and carrying out some simple computation:

$$\sum_{jkl} (c_{ijkl} K_j K_l - \rho \omega^2 \delta_{ik}) u_k^0 = 0 \quad (2.2.3-9)$$

Now define  $K_j = K \cos(\theta_j) = K n_j$ , where  $n_j$  is the cosine of the angle between  $\vec{K}$  and the  $x_j$  axis; moreover,  $\vec{n}$  is the unit vector along the  $\vec{K}$  direction, which means  $n_1^2 + n_2^2 + n_3^2 = 1$ . Thus, substituting this definition into the eq. (2.2.3-9) gives:

$$\sum_{jkl}(c_{ijkl}n_jn_l \cdot K^2 - \rho\omega^2\delta_{ik})u_k^o = 0 \quad (2.2.3-10)$$

By recalling some basic concepts of waves, we can derive that

$$\frac{\omega}{K} = \frac{2\pi/T}{2\pi/\lambda} = \frac{\lambda}{T} = v \quad (2.2.3-11)$$

Dividing the eq. (2.2.3-10) by  $K^2$ , we have

$$\sum_{jkl}(c_{ijkl}n_jn_l - \rho v^2\delta_{ik})u_k^o = 0 \quad (2.2.3-12)$$

Then the wave equation for plane wave solutions has become a set of linear equations.

If we note the term  $c_{ijkl}n_jn_l$  as  $\Gamma_{ik}$ , we can rewrite eq. (2.2.3-12) like:

$$\begin{pmatrix} \Gamma_{11} - \rho v^2 & \Gamma_{12} & \Gamma_{13} \\ \Gamma_{12} & \Gamma_{22} - \rho v^2 & \Gamma_{23} \\ \Gamma_{13} & \Gamma_{23} & \Gamma_{33} - \rho v^2 \end{pmatrix} \begin{pmatrix} u_1^o \\ u_2^o \\ u_3^o \end{pmatrix} = 0 \quad (2.2.3-13)$$

The condition for a nontrivial solution for this equation is that the determinant of the coefficient of the  $u_k^o$  should be zero, which gives:

$$\begin{vmatrix} \Gamma_{11} - \rho v^2 & \Gamma_{12} & \Gamma_{13} \\ \Gamma_{12} & \Gamma_{22} - \rho v^2 & \Gamma_{23} \\ \Gamma_{13} & \Gamma_{23} & \Gamma_{33} - \rho v^2 \end{vmatrix} = 0 \quad (2.2.3-14)$$

Now let us look back to the section 2.2.2. If we take the elastic constant matrix of a cubic crystal into account, the Christoffel equation for cubic symmetry becomes [10]:

$$\begin{pmatrix} n_1^2 c_{11} + (n_2^2 + n_3^2) c_{44} - \rho v^2 & n_1 n_2 (c_{12} + c_{44}) & n_1 n_3 (c_{12} + c_{44}) \\ n_2 n_1 (c_{12} + c_{44}) & n_2^2 c_{11} + (n_3^2 + n_1^2) c_{44} - \rho v^2 & n_2 n_3 (c_{12} + c_{44}) \\ n_3 n_1 (c_{12} + c_{44}) & n_3 n_2 (c_{12} + c_{44}) & n_3^2 c_{11} + (n_1^2 + n_2^2) c_{44} - \rho v^2 \end{pmatrix} \begin{pmatrix} u_1^o \\ u_2^o \\ u_3^o \end{pmatrix} = 0 \quad (2.2.3-15)$$

For isotropic case, we can just take a simple example of the propagation along the  $x_1$  direction, which means  $n_1 = 1$  and  $n_2 = n_3 = 0$ . Then we substitute these conditions into the previous equation and let the determinant of the coefficient of the  $u_k^o$  equals 0:

$$\begin{vmatrix} c_{11} - \rho v^2 & 0 & 0 \\ 0 & c_{44} - \rho v^2 & 0 \\ 0 & 0 & c_{44} - \rho v^2 \end{vmatrix} = 0 \quad (2.2.3-16)$$

We will get three eigenvalues for this equation:  $c_{11} = \rho v^2$ ,  $c_{44(1)} = \rho v^2$ ,  $c_{44(2)} = \rho v^2$ .

Let us take a look at it deeply:

[8] For the first eigenvalue,  $c_{11} = \rho v^2$ . If we substitute it back into eq. (2.2.3-15), we will find that

$$\begin{cases} 0u_1^o = 0 \\ (c_{44} - c_{11})u_2^o = 0 \\ (c_{44} - c_{11})u_3^o = 0 \end{cases} \quad (2.2.3-17)$$

Resulting in  $u_2^o = u_3^o = 0$  with no restriction on  $u_1^o$ . The direction of particle motion is along the  $x_1$  axis as is the direction of travel of the wave, so this is a longitudinal wave with speed

$$v_l = \sqrt{\frac{c_{11}}{\rho}} \quad (2.2.3-18)$$

For the second and third eigenvalues,  $c_{44} = \rho v^2$ . Just similar to the previous analysis, it gives  $u_1^o = 0$  with no restrictions on  $u_2^o$  or  $u_3^o$ . The displacements of  $u_2^o$  and  $u_3^o$  are normal to the direction of the wave propagation, and thus represent transverse waves along the  $x_2$  or  $x_3$  axis with speed

$$v_t = \sqrt{\frac{c_{44}}{\rho}} \quad (2.2.3-19)$$

Due to the isotropic character, this result is pervasive to the isotropic material. Recalling from the conclusion (eq. (2.2.2-18)) we drew in the last section, we can obtain a very useful formula that can be used to reveal the relationship between the Young's modulus of the isotropic material and the velocities of waves propagating through it:

$$E = \rho v_t^2 \frac{3v_l^2 - 4v_t^2}{v_l^2 - v_t^2} \quad (2.2.3-19)$$

With this equation, we have an opportunity to evaluate the Young's modulus of an isotropic material by testing the velocities of the longitudinal and transverse waves applied on it.

#### 2.2.4 Ratio of the velocity of Rayleigh wave and transverse wave

From the previous section, we can see that if we can measure the sample's density, the velocity of the longitudinal and transverse wave at the same time, we are able to easily calculate the Young's modulus and other elastic properties of the sample. However, we cannot measure the velocity of the transverse wave directly by using only one transducer. Therefore, we need to find other ways to figure out the transverse wave's speed by measuring the velocity of the Rayleigh wave and building a relationship between them.

Fortunately, Viktorov [6] established a relationship among the velocity of the surface Rayleigh wave, the longitudinal wave, and the transverse wave, so that we can derive any one of them from the other two.

Recalling from the eq. (2.2.1-23), if we let the real and imaginary part be equal to zero, it reduces to the form:

$$\left(\frac{v_R}{v_t}\right)^6 - 8\left(\frac{v_R}{v_t}\right)^4 + 8\left[3 - 2\left(\frac{v_t}{v_l}\right)^2\right]\left(\frac{v_R}{v_t}\right)^2 - 16\left[1 - \left(\frac{v_t}{v_l}\right)^2\right] = 0 \quad (2.2.4-1)$$

If we define  $\left(\frac{v_R}{v_t}\right)^2$  as  $R$ , then we can rewrite this equation in another form, which is sometimes called the Rayleigh equation to memorize Lord Rayleigh in 1885:

$$R^3 - 8(R - 1)(R - 1 - c_{12}/c_{11}) = 0 \quad (2.2.4-2)$$

As we know that  $c_{12}/c_{11}$  can be treated as the Poisson's ratio  $\nu$ , which is ranging between 0 and 0.5 for most materials. If we plot the two functions:  $f_1(R) = R^3/8$  and  $f_2(R) =$

$(R - 1)(R - 1 - c_{12}/c_{11})$  in Matlab<sup>2</sup>, and changing the range of  $c_{12}/c_{11}$  from 0 to 0.5. We will find out that the positive real root locates between 0.764 and 0.869. Therefore, the ratio  $\frac{v_R}{v_t} = \sqrt{R}$  ranges from 0.874 to 0.9325. This ratio's range is a very important judgement criterion in our following measurement to exclude the extraneous roots of the transverse wave's velocity.

### 2.3 RESEARCH HISTORY

In 1970s, lots of researchers devoted themselves on expanding the application fields of ultrasonic transducer systems based on the development of a mechanically scanned acoustic microscope [11]. It was found in 1977 that the curve  $V(z)$ , which represented the output of a piezoelectric transducer, varied significantly with the distance between the acoustic probe and the surface of the sample [12]. After that, the relationship between the intervals in  $V(z)$  and the velocity of the Rayleigh surface wave was revealed by Parmon and Bertoni [13] in 1979.

Although this great achievement made it possible to measure the acoustic properties quantitatively, the principle of the point-focus system (using a spherical lens with which a plane wave radiating from the transducer is circularly focused into a point) had a disadvantage to excite leaky surface acoustic wave propagating in all directions [14]. In order to detect the acoustic properties of both isotropic and anisotropic materials, a linearly focused acoustic beam was proposed by Kushibiki et al. in 1981 [15]. Subsequently, the following studies were based on this design of transducers.

---

<sup>2</sup> For details, see the Appendix B

The design of the transducer system in this study also refers to this type. A linearly focused lens-less polyvinylidene fluoride (PVDF) transducer which offers 10 MHz central frequency is chosen from the comparison of the previous works.

## 2.4 PRINCIPLE OF MEASUREMENT

### 2.4.1 Snell's Law and critical angle

Since we want to use the Rayleigh wave to help characterize the elastic properties, we have to learn how to excite the Rayleigh wave at first. As we know, when a wave comes across an interface of two different material, part of it reflects and part of it refract at its own unique angle. It is worth to notice that the refraction takes place between two materials with the different acoustic velocities. [2] When a wave encounters the interface of two different kinds of materials, a portion of it will propagate at a different speed other than it in the previous material. Consequently, this reason changes the direction of the wave's propagation so that it looks like "bent".

As we can see from the figure below, let us notate the incident angle as  $\theta_i$  and the refraction angle as  $\theta_r$ . According to the Snell's Law, we have:

$$\frac{\sin \theta_i}{v_i} = \frac{\sin \theta_r}{v_r} \quad (2.4.1-1)$$

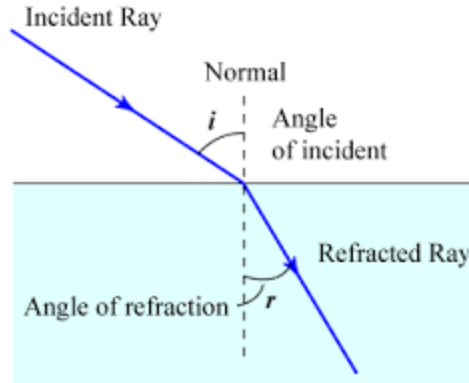


**Figure 8.** The wave's refraction

It is worth noting that the incident or refraction angle is proportional to the velocity of the propagating at its side since the sinusoidal function possesses monotonicity in the range from 0 to  $\pi/2$ . Another detail that deserves to be taking care of is that only when the refraction takes place from the material with lower propagating velocity to the material with higher velocity, we have an opportunity to let the refraction angle become  $\pi/2$  before the incident angle turns to  $\pi/2$ .

Because the transverse wave does not propagate as faster as the longitudinal wave, it does also not refract as much as the longitudinal wave does. In the meantime, the ultrasonic we used in the experiment is usually combined with both transverse wave and longitudinal wave. As a result, we have two different refraction angles for the longitudinal wave and the transverse wave respectively. When a combined wave propagates from a slower to a faster material, there is an incident angle letting the refraction angle of the longitudinal wave become  $\pi/2$  (At this time, the refraction angle of the transverse wave is less than  $\pi/2$  due to the slower traveling velocity); as the incident angle increases, at some moment, there is another incident angle that makes the angle of the transverse wave's refraction to become  $\pi/2$  as well. The former is called "the first critical angle". And the latter is called "the second critical angle". As we introduced before, the surface Rayleigh wave can be treated as a combination of a longitudinal wave and a transverse

wave. Therefore, the Rayleigh wave can only be generated slightly beyond the second critical angle.

In conclusion, the concave probe of the PVDF transducer we used in the following measurement covers almost  $110^\circ$ , which is greater than the second critical angle, so that the surface wave can be excited.

#### **2.4.2 Time-resolved Defocusing Method**

As mentioned before, a bunch of measurements taking advantages of the relationship between the dip interval and Rayleigh wave velocity were conducted after the significance discovered by Permon et al. These techniques, however, required a strict mechanical precision of the driving system that might reflect on the scanning of an acoustic lens or sample. It was difficult to apply this technique in which rapidity and easy-manipulation were required [16].

To eliminate this restriction, Yamanaka proposed a more direct way to measure the Rayleigh wave velocity without z scanning called time-resolved defocusing method [16]. In this method, he utilized the difference of traveling time between the axial wave and leaky surface wave, which were easily observed from the output signal, to calculate the velocity of Rayleigh wave  $-v_R$ .

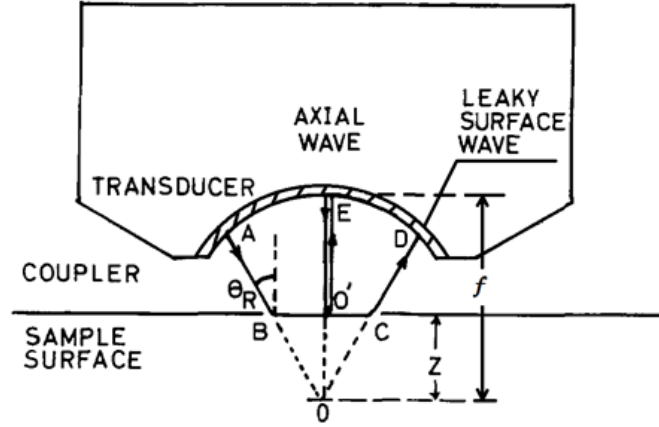


**Figure 9.** Working principle of concave transducer [16]

The principle of the measurement is shown in Figure 8. The axial wave propagates along the path EO'E, while the surface Rayleigh wave excited at angle  $\theta_R$  goes through the path ABO'CD. Therefore, the traveling time of the axial wave is:

$$T_A = \frac{2(f-z)}{v_w} \quad (2.4.2-1)$$

where  $v_w$  is the velocity of the wave propagating in the water as coupler.

And the traveling time of the Rayleigh wave is:

$$T_R = \frac{2\left(f - \frac{z}{\cos \theta_R}\right)}{v_w} + \frac{2(\tan \theta_R) \cdot z}{v_R} \quad (2.4.2-2)$$

where  $v_R$  is the velocity of the Rayleigh wave on the sample surface.

Solving the eq. (2.4.2-1) and (2.4.2-2) simultaneously, we can have

$$t = T_R - T_A = \frac{2z(1 - \cos \theta_R)}{v_w} \quad (2.4.2-3)$$

by eliminating  $v_R$  with the relation

$$\frac{v_w}{v_R} = \frac{\sin \theta_R}{\sin 90^\circ} \quad (2.4.2-4)$$

From the eq. (2.4.2-3) we can find that the distance  $z$  and the time interval  $t$  are linearly dependent, since  $\cos \theta_R$  and  $v_w$  are both established constant. The linear relationship between the distance  $z$  and the time interval  $t$  can be described as follows:

$$\frac{dz}{dt} = \frac{v_w}{2(1-\cos \theta_R)} \quad (2.4.2-5)$$

In the meanwhile, we can derive from the Snell's Law that

$$v_R = \frac{v_w}{\sin \theta_R} = \frac{v_w}{\sqrt{1-\cos^2 \theta_R}} \quad (2.4.2-6)$$

Eliminate  $\cos \theta_R$  by substituting eq. (2.4.2-5), then we get

$$v_R = \left[ \frac{1}{v_w \left(\frac{dz}{dt}\right)} - \frac{1}{4 \left(\frac{dz}{dt}\right)^2} \right]^{-1/2} \quad (2.4.2-7)$$

where  $v_w = 1480 \text{ m/s}$ , the velocity of the acoustic wave in distilled water.

From the above, it can be concluded that the velocity of the Rayleigh surface wave is able to be calculated using the Eq. (2.4.2-7) by measuring the slope regarding the time interval  $t$  and the corresponding defocusing position  $z$ .

### 2.4.3 Chemical Corrosion

As we know, there are many kinds of metallic corrosion existing in our daily life and industry. But the commonest one is electrochemical corrosion which is under the conditions of galvanic cell (including an anode and a cathode), electrolyte and closed circuit. For example, when a metal is placed in the moist atmosphere, it forms a water film on the surface which includes a small quantity of hydrogen ions, hydroxyl ions, and dissolved oxygen. As a result, this moisture film works like the electrolyte. Combining with the metal itself and the impurity elements (e.g.

carbon or other nobler element) in this metal, it becomes numerous tiny galvanic cells on the surface of the metal. In each galvanic cell, active metal works as the anode where the oxidation reaction takes place; inert element works as the cathode at which the reduction reaction happens.

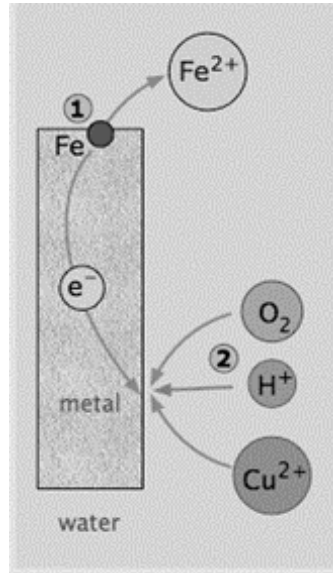


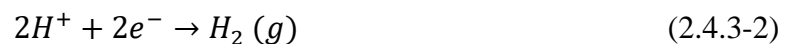
**Figure 10.** Electrochemical Corrosion in Active Metal [17]

The electrons transfer in this process accelerates the reduction-oxidation reaction, that is the reason why the electrochemical corrosion is faster and severer than the general chemical corrosion. The corrosion can be separated into two parts according to whether it gets electrons or not. As shown in Fig. 2, the relatively active metal (Fe in this example) which loses negative charges in the oxidizing process becomes ferrous ion. The reaction equation at the anode is:



Then the metal ions dissolve in the moisture film and the electrons migrate to the cathode where they are taken up by a depolarizer [17] :

Hydrogen evolution corrosion:



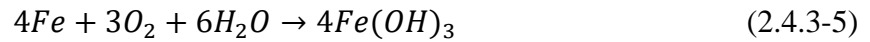
Oxygen absorption corrosion:



Other nobler metal:



Because oxygen exists almost anywhere in the atmosphere and it can be lightly dissolved in a thin film of adsorbed moisture, the oxygen absorption corrosion is more commonly seen than the hydrogen evolution corrosion. Moreover, the oxygen absorption corrosion could happen in faintly acidic, neutral or alkaline environment. Thus, the large amounts of electrochemical corrosion in the air are oxygen absorption corrosion. The total reaction equation of it is (taking iron for example):



Since the corrosion reaction changes the component and its molecular structure on the surface of the metal, which can be sensitively detected by the Rayleigh surface wave, we can estimate the elastic property by measuring the variation of the Rayleigh wave's velocity.

### **3.0 EXPERIMENTAL PROCEDURE**

From the previous theoretical analysis, we are clear now that the objective of this experiment is to measure the density of the sample and the defocus-length with regards to traveling time so that we can calculate the velocity of the Rayleigh wave. After that, we will estimate the velocity of the longitudinal wave by measuring the thickness of the sample and the round-trip traveling time of the longitudinal wave's propagation. Finally, we can solve the elastic property – Young's modulus, by means of deriving the velocity of the transverse wave from the velocities we indirectly measured in this experiment.

#### **3.1 EQUIPMENT SET-UP**

As mentioned in the last chapter, the design of the transducer system mainly refers to the work of Yamanaka [16] and D. Xiang [18].

In this measurement, a PVDF thin film is attached to a cylindrical concave surface as the testing probe at the terminal of the stage. The concave's focal distance is 35mm and its aperture half angle is 50 degrees. The interior of the concave is filled up with tungsten powder and epoxy with a weight ratio of 2:1 as high impedance backing material. The stage is controlled by a programmed stepping motor (SURUGA SEIKI CO., LTD, Shizuoka, Japan) so that the defocus process of the PVDF probe can be precisely controlled. Connected to the pulser/receiver

(5072PR, OLYMPUS), the PVDF transducer can emit and receive the ultrasonic signal through the couplant – distilled water and convert it into an electric signal, which can be easily analyzed. The received signal is sent to an oscilloscope (4034A, AGILENT TECHNOLOGIES) where we can observe and record the variation of the waveform. The schematic diagram of the Line-Focus Ultrasonic Testing System used in this test is shown in Figure 10.

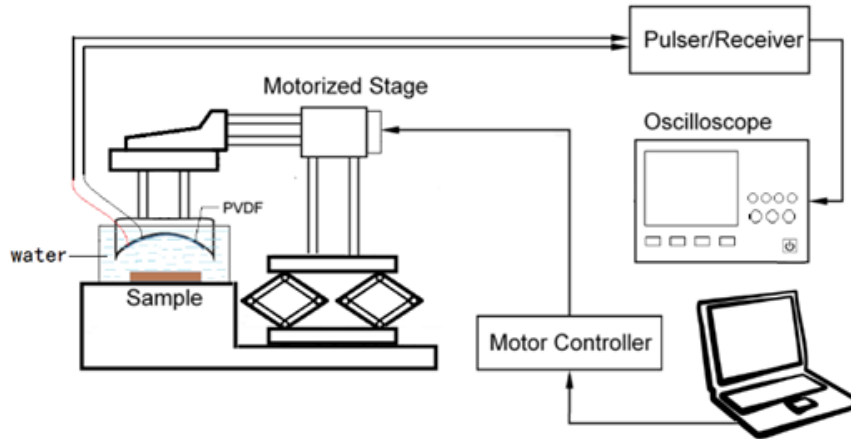


**Figure 11.** Schematic diagram of the Ultrasonic Testing System

### 3.2 PREPARATION OF SAMPLES

In this test, we choose the standard stainless steel and additive manufactured steel SS420 as samples. Connecting with copper, the samples are immersed in the electrolyte solution for 10 days, and 30 days respectively. To aggravate the chemical attack, we pump air and add nitric acid into the solution.

One comparison of the samples before and after the process is shown in Figure 12 and 13. And Figure 14 shows the galvanic corrosion in process.



**Figure 12.** Samples before corrosion



**Figure 13.** Samples after corrosion

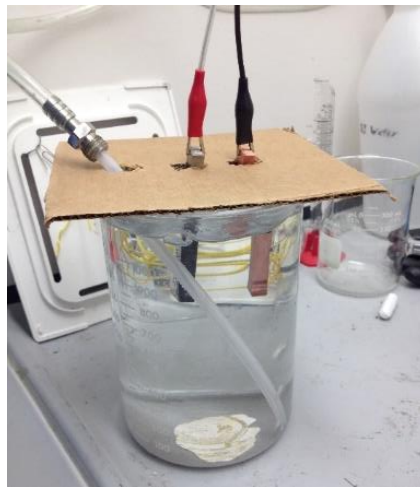


**Figure 14.** The process of the corrosion

### 3.3 MEASUREMENT OF THE DENSITY

Since the samples we used in this experiment are standard samples, which means we can look up for its original density directly on the internet. For example, the density of the annealed SS 420 product from McMaster-Carr is  $\rho = 7750 \text{ kg/m}^3$  and the density of the additive manufactured sample from ExOne™ M-Flex is  $\rho = 7860 \text{ kg/m}^3$  [19].

As the experiment carries on, the corrosion will change not only the components beneath the surface of the sample but also the whole mass of the sample due to the rust formation and the eroded material's detachment. Especially for the additive manufactured sample, the variation of the density is conspicuous because the chemical binder is vulnerable during the corrosion. Thus, we need to measure the density of the additive manufactured material after the artificial corrosion process.

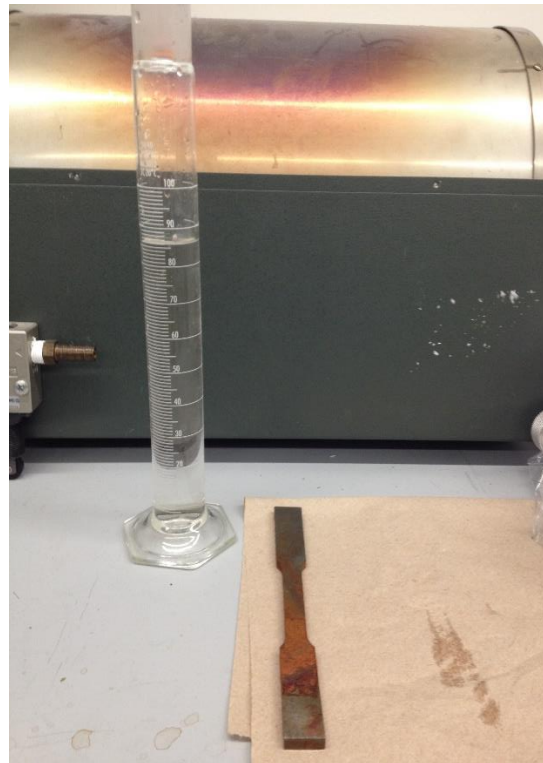


**Figure 15.** Measurement of the sample's volume by drainage method

We used the drainage method to estimate the volume of the sample once it got dried from the electrolytic bath. As the figure shown above, the volume of the drained water is 84.4 ml. After we measured the mass of the corroded sample, we can calculate the density of the sample after corrosion by using the formula:  $\rho = m/V$ .

### 3.4 DATA RECORDING DURING TIME-RESOLVED DEFOCUSING

At the beginning of the measurement, we need to adjust the stage to find out the focal position where the amplitude of the output voltage is largest. During this calibration, ensure the surface of the sample remaining horizontal as much as possible so that the energy of the signals reflecting from the sample can be strong enough to be received by the transducer. The waveform at the focal position is shown in the figure below.

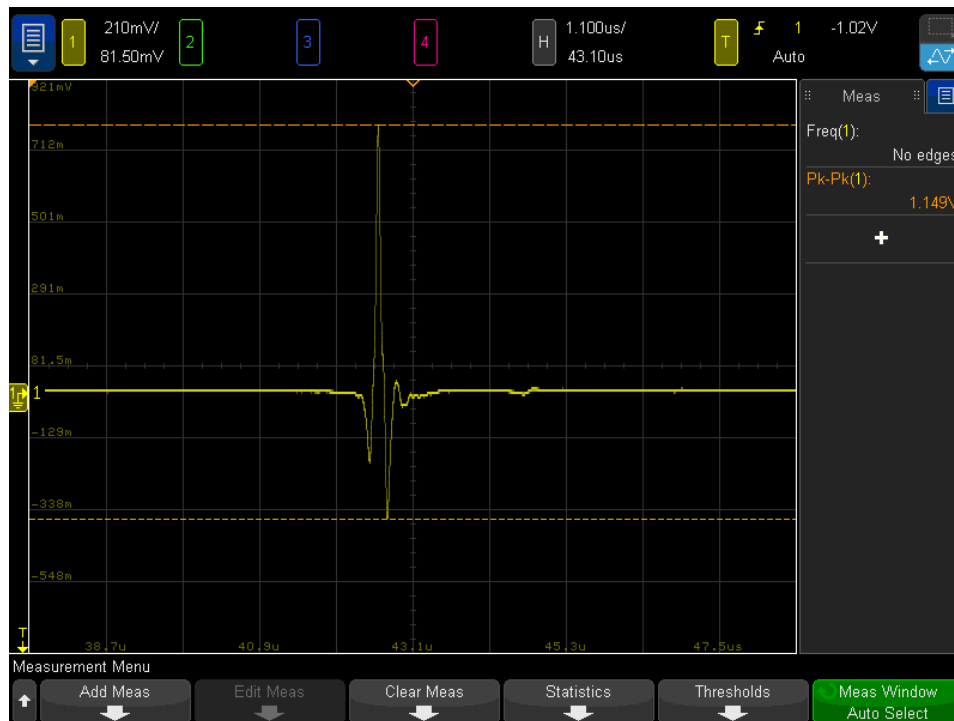
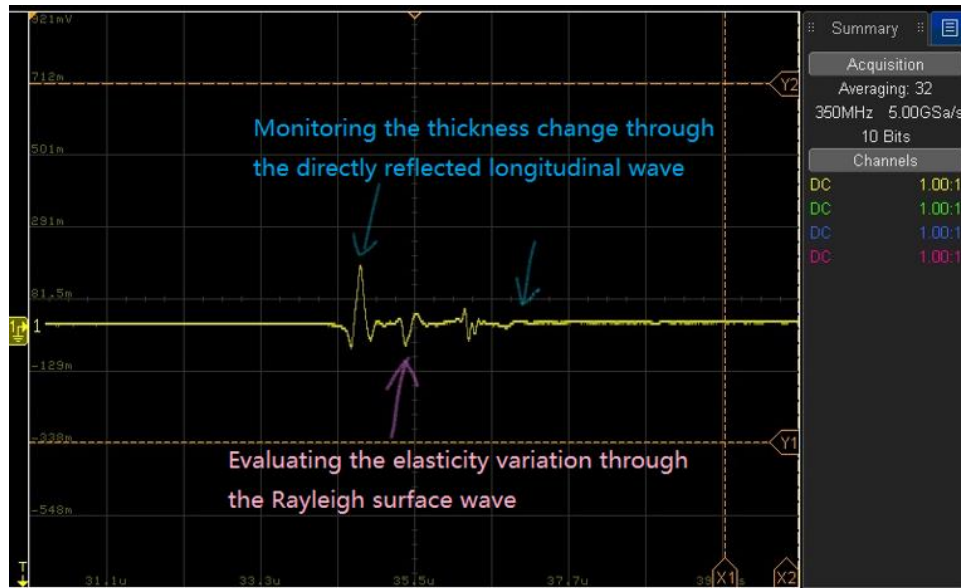


Figure 16. Waveform at the focal position

From the figure above, we can see that the largest crest is the wave reflected from the surface of the sample directly. Since the energy is very concentrated, the crest of this wave at the focal position is extremely high. The second very tiny crest on this figure indicates that there is a wave reflecting from the bottom of the sample. Due to the energy consumption in many times propagation between different materials, the crest of this wave we can observe on the oscilloscope is not that obvious. At this focal position, we denote it as the original position of  $z$ , that is,  $z = 0$ .

As the transducer gets close to the sample, the waves begin to separate from each other progressively. In the figure shown below, we can see that the first crest still represents the axial wave reflecting from the surface of the sample; the second wave (which separates from the first one slower than the wave on its right side) is the Rayleigh wave (highlighted by the pink color arrow); the distance between the crest of the first wave and the crest of the last tiny wave (highlighted by the blue color arrows) has not changed since the thickness of the sample is the same.



**Figure 17.** Waveform during the defocus process

As the defocusing keeps going, we can record the corresponding time difference between the peak of the axial wave and the peak of the Rayleigh wave at each step. Recording about 10 sets of data, we can draw them on a diagram. After using a linear trendline to fit these divergent points, we can have a relationship of position  $z$  with regards to traveling time  $t$ .

## 4.0 DATA PROCESSING AND RESULTS

Once the testing system was set up, we could calibrate the stage to the focal position where the amplitude of the output voltage we observed on the oscilloscope was the largest. Subsequently, we defocused the motorized stage 0.2mm per step in z-direction. Then we recorded the position value  $z$  and the corresponding traveling time of the axial waves and the Rayleigh wave at each step. After that, we could depict points on the Cartesian coordinate and use a linear trendline to fit them, so that the slope of the trendline was the value  $dz/dt$  that we would need in Rayleigh wave's speed calculation.

### 4.1 RESULTS OF THE STANDARD SAMPLE

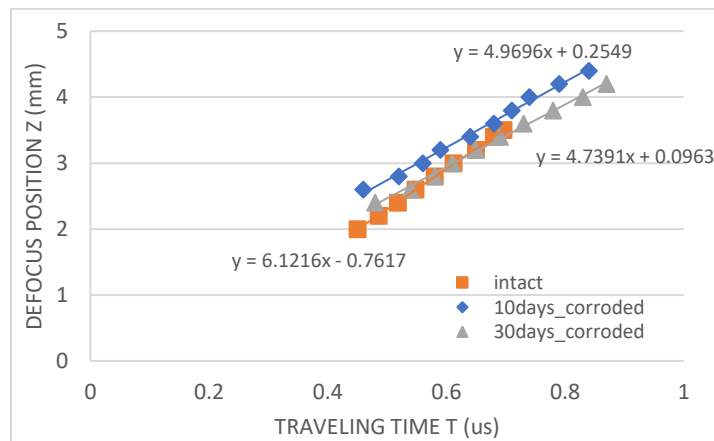


**Figure 18.** Defocus-length with respect to traveling time of standard samples

From the figure above, we can see that the values of  $dz/dt$  (the slope of the trendline) for the uncorroded, 10 days corroded, and 30 days corroded status are 6.1216, 4.9696, and 4.7391 respectively. Based on these values, we can begin calculating the velocity of the Rayleigh wave and deriving the other parameters and elastic properties as listed below.

**Table 1.** Parameters and Elastic Properties' Calculation of Standard Samples

	dz/dt	* $v_w$ (m/s)	* $v_R$ (m/s)	* $v_l$ (m/s)	* $v_t$ (m/s)	$\rho$ (kg/m <sup>3</sup> )	E(Gpa)
intact	6.1216	1480	3105.285	5403.509	3417.719	7750	211.214
10d-corroded	4.9696	-	2818.982	4791.667	3128.002	7612	168.128
30d-corroded	4.7391	-	2758.232	4618.182	3082.175	7584	158.274

As we can see from Table 1, the velocity of the Rayleigh wave, which can be calculated according to the eq. (2.4.2-7), becomes smaller after the sample is corroded. Then, the longitudinal wave can be obtained by using formula  $v_l = 2\delta/t$ , where  $\delta$  is the thickness of the sample and  $t$  is the traveling time in the sample back and forth.

Referring to the equation proposed by D. Royer and E. Dieulesaint [20], we can calculate the shear wave's velocity by solve the cubic equation as follows:

$$\left(\frac{v_t}{v_R}\right)^3 - \left(\frac{v_t}{v_R}\right)^2 - 0.718 \left(\frac{v_l}{v_R}\right)^2 \left(\frac{v_t}{v_R}\right) + \frac{3}{4} \left(\frac{v_l}{v_R}\right)^2 = 0 \quad (4.0-1)$$

Obviously, there are three roots after solving a cubic equation. We can easily exclude the negative root because it is not in accord with the common sense. Recalling from the criterion we drew in section 2.2.4, we can exclude another root that is out of the range -  $v_R/v_t$  is between 0.874 and 0.9325. The remaining root is the solution of the transverse wave we are seeking for in this experiment.

Therefore, the change of the elastic properties can be calculated based on the variation of the surface, longitudinal and shear wave's speed [2]. Using the drainage method, we can measure the density of the sample. Finally, by recalling the formula Eq. (2.2.3-19), we can characterize the Young's modulus of the standard SS 420 sample under different corrosion conditions.

Compared to the official material data in table 2, we can figure out that the uncorroded sample's elastic property measured by the line-focused ultrasonic transducer quite match its original data.

**Table 2.** Stainless Steel Grade 420 Typical Material Properties

Material Properties		Value
Constituent (%)	Carbon	0.15 – 0.46
	Iron	82.1 –87.15
	Manganese	0.40 – 1.00
	Phosphorus	0 – 0.04
	Sulfur	0 – 0.03
	Chromium	12.00 – 14.00
Density (kg/m <sup>3</sup> )		7750
Elastic Modulus (GPa)		200

## 4.2 RESULTS OF THE ADDITIVE MANUFACTURED SAMPLE

For the additive manufactured sample, the analysis is similar. We are able to draw a diagram about  $dz/dt$  like the previous sample. Unfortunately, the waveform of the sample under 30 days

corrosion is too weak to distinguish the Rayleigh wave from other surface waves, which will be discussed in the following section. In figure 19, we can obtain the value of  $dz/dt$  which can be used in velocity of transverse wave calculation.

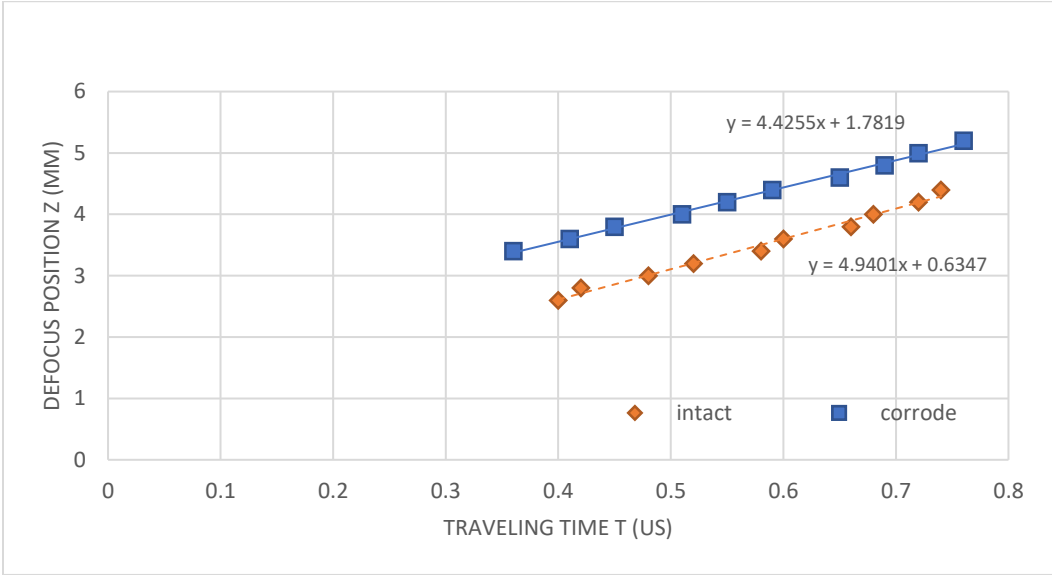


**Figure 19.** Defocus-length with respect to traveling time of additive manufactured samples

From table 3, we can also conclude that the velocity of the Rayleigh wave becomes smaller after the sample is corroded. Accordingly, the velocities of the longitudinal and transverse waves decrease as well.

**Table 3.** Parameters and Elastic Properties’ Calculation of Additive Manufactured Samples

	$dz/dt$	$*v_w$ (m/s)	$*v_R$ (m/s)	$*v_l$ (m/s)	$*v_t$ (m/s)	$\rho$ (kg/m <sup>3</sup> )	E(Gpa)
uncorroded	4.9401	1480	2811.278	5342.593	3039.401	7860	183.086
10d-corroded	4.4255	1480	2673.443	4803.279	2918.747	6933.3	142.619

In a similar way, the change of the elastic properties can be calculated based on the variation of the surface, longitudinal and shear wave’s speed.

## 5.0 DISCUSSION AND CONCLUSION

From the previous analysis, it can be concluded that as the corrosion becomes severer the velocity of the Rayleigh wave we detect becomes slower. What's more, the Young's modulus we calculated based on the measurement becomes smaller as well. If we compare the corroded standard samples' elastic properties with the data given by D. Chicot et al. [21], we will notice that they are close to the mechanical property of magnetite ( $\text{Fe}_3\text{O}_4$ ). The result coincides well with the color of the corroded layer we observed from figure 13 because the magnetite (also known as ferrous-ferric oxide) is black or brownish-black.

For the additive manufactured sample case, similar conclusion can be drawn. The velocity of the Rayleigh wave and Young's modulus decrease at some degree after getting corroded. This phenomenon can be explained by the reduction of the stiffness constants. However, the sample after 30 days corrosion can hardly be tested, since the surface roughness becomes too large. A longer wavelength ultrasonic wave would be suggested to apply into the future measurement.

In conclusion, characterization of the additive manufacture metal alloys' corrosion by PVDF line focused ultrasonic transducer system was conducted in this study. Compared to the additive manufactured stainless steel, the corrosion evaluation of the traditional manufactured sample is more feasible and practical.

## **6.0 EXPERIMENT IMPROVEMENT AND FUTURE WORK**

### **6.1 THE VULNERABLE STEEL TYPE**

The steel type used in this experiment is stainless steel grade 420. As a kind of stainless steel, it usually contains 10-20% chromium which is the main element for resistance to corrosion. With over 11% chromium, steel is about 200 times more resistant to corrosion than general mild steel.[22] Thus, in our future improvement, we can consider to use some mild steel containing less chromium elements instead of using the stainless steel so that we were able to obtain a thorough corrosion and the corrosion could be accelerated.

### **6.2 THE PATTERNS OF CORROSION**

Through our samples preparation and the whole experiment, the samples underwent mostly the uniform corrosion with low amounts of roughness. However, in the real situation, the corrosions happened on the surface of the marine vessels are pitting corrosion in most cases. The most challenging thing is that the non-uniform corrosion with high surface roughness raise a higher requirement to feasibility and reliability of the ultrasonic measurement since the roughness of the surface might cause an effect to the precise of the measurement results.

### **6.3 THE PORTABILITY OF THE LINE-FOCUSED TRANSDUCER SYSTEM**

To eliminate the limitation of the line-focused transducer system operating in laboratory environment, it is worthwhile to attempt to build a chamber with the PVDF probes. Then the chamber is filled up with the coupling medium, such as distilled water, silicone oil, and *etc.* If this idea is able to be realized, it could be a promising way to expand the applications of this transducer system to a more practical field. And the measurement will become easier to take due to the improvement in portability and integrity of this system.

## APPENDIX A

### VOIGT NOTATION

The generalized form of Hooke's Law is:

$$\sigma_{ij} = \sum_{kl} c_{ijkl} \varepsilon_{kl} \quad (\text{A-1})$$

The index  $ijkl$  count from 1 through 3 to represent three directions in a true space. And the coefficients  $c_{ijkl}$  are components of the stiffness tensor. According to the knowledge of permutation and combination, we can easily figure out that there are  $3^4 = 81$  of the coefficient  $c_{ijkl}$ . Fortunately, even in the most general case, there are many symmetry relations among the  $c_{ijkl}$  reducing the number of independent  $c_{ijkl}$  considerably, since the tensors  $\sigma_{ij}$  and  $\varepsilon_{kl}$  are symmetric so that the coefficient makes no difference if the first two or last two subscripts are interchanged. That means:  $c_{ijkl} = c_{jikl}$  and  $c_{ijkl} = c_{ijlk}$ . This symmetry under the interchange of indices make possible a considerable simplification with the change in notation, often known as the Voigt Notation.

So we can notate them in a different way: [7]

$$\begin{aligned} (1,1) &\leftrightarrow 1 \quad (2,2) \leftrightarrow 2 \quad (3,3) \leftrightarrow 3 \\ (2,3) = (3,2) &\leftrightarrow 4 \quad (1,3) = (3,1) \leftrightarrow 5 \quad (1,2) = (2,1) \leftrightarrow 6 \end{aligned} \quad (\text{A-2})$$

For examples,

$$c_{14} = c_{1123} = c_{1132} \quad (\text{A-3})$$

$$c_{45} = c_{2313} = c_{2331} = c_{3213} = c_{3231}$$

This Voigt Notation can be extended to the stresses and strains so that Eq. (A-1) becomes:

$$\sigma_m = \sum_{n=1}^6 c_{mn} \varepsilon_n \quad (\text{A-4})$$

It is supposed to be noticed that for stresses tensor,  $\sigma_m \leftrightarrow \sigma_{ij}$  as the notation of the elastic coefficient; however, for strains tensor, the situation becomes more complicated. The notation of strains should be defined as:

$$\varepsilon_1 \leftrightarrow \varepsilon_{11} \quad \varepsilon_2 \leftrightarrow \varepsilon_{22} \quad \varepsilon_3 \leftrightarrow \varepsilon_{33} \quad (\text{A-5})$$

$$\varepsilon_4 \leftrightarrow 2\varepsilon_{23} \quad \varepsilon_5 \leftrightarrow 2\varepsilon_{13} \quad \varepsilon_6 \leftrightarrow 2\varepsilon_{12}$$

With the results, the expansion for  $\sigma_{11}$  may be written as:

$$\sigma_1 = c_{11}\varepsilon_1 + c_{12}\varepsilon_2 + c_{13}\varepsilon_3 + c_{14}\varepsilon_4 + c_{15}\varepsilon_5 + c_{16}\varepsilon_6 \quad (\text{A-6})$$

Whose original expression should be:

$$\sigma_{11} = c_{1111}\varepsilon_{11} + c_{1122}\varepsilon_{22} + c_{1133}\varepsilon_{33} + 2c_{1123}\varepsilon_{23} + 2c_{1131}\varepsilon_{31} + 2c_{1112}\varepsilon_{12} \quad (\text{A-7})$$

Hooke's Law can also be written inversely to express the strains in terms of stresses:

$$\varepsilon_{ij} = \sum_{kl} s_{ijkl} \sigma_{kl} \quad (\text{A-8})$$

Similarly, it can be expressed in this term:

$$\varepsilon_m = \sum_{n=1}^6 s_{mn} \sigma_n \quad (\text{A-9})$$

However, because of the factor 2 of  $\varepsilon$ , the notation of  $s_{mn}$  becomes further complicated.

For example, for the expression of  $\varepsilon_{23}$ :

$$\varepsilon_{23} = s_{2311}\sigma_{11} + s_{2322}\sigma_{22} + s_{2333}\sigma_{33} + 2s_{2323}\sigma_{23} + 2s_{2331}\sigma_{31} + 2s_{2312}\sigma_{12} \quad (\text{A-10})$$

When we apply the Matrix Notation, we should also take  $\varepsilon_4 \leftrightarrow 2\varepsilon_{23}$  into consideration.

Thus, we have:

$$\varepsilon_4 = s_{41}\sigma_{11} + s_{42}\sigma_{22} + s_{43}\sigma_{33} + s_{44}\sigma_{23} + s_{45}\sigma_{31} + s_{46}\sigma_{12} \quad (\text{A-11})$$

Where

$$s_{41} = 2s_{2311}, s_{42} = 2s_{2322}, s_{43} = 2s_{2333}, \quad (\text{A-12})$$

$$s_{44} = 4s_{2323}, s_{45} = 4s_{2331}, s_{46} = 4s_{2312}$$

In general, if  $p$  is the amount of subscripts greater than 3 in the pair  $(m, n)$ , then

$$s_{mn} = 2^p s_{ijkl} \quad (\text{A-13})$$

## APPENDIX B

### RATIO OF $V_R/V_S$ ANALYSIS IN MATLAB

Recalling the Rayleigh equation, we have:

$$R^3 - 8(R - 1)(R - 1 - c_{12}/c_{11}) = 0 \quad (\text{B-1})$$

As we know that  $c_{12}/c_{11}$  can be treated as the Poisson's ratio  $\nu$ , which is ranging between 0 and 0.5 for most materials. Let us assume that  $f_1(R) = R^3/8$  and  $f_2(R) = (R - 1)(R - 1 - c_{12}/c_{11})$ , where the range of  $c_{12}/c_{11}$  is from 0 to 0.5. If we let these two functions be equivalent, the points of intersection of these two functions should be the solution to eq. (B-1).

The MATLAB code and the corresponding figure are shown as follows:

```

Editor - D:\My Document\2016 Spring Term\OneDrive\2017 Spring Term\Thesis\motor control I\Range.m
EDITOR PUBLISH VIEW
Range.m x +
1 - R = [0:0.001:1.3];
2 - f1 = R.^3/8;
3 - f2 = (R-1).^2;
4 - f3 = (R-1).*(R-1.5);
5 - i = find(abs((f1-f2))<0.0004);
6 - j = find(abs((f1-f3))<0.0006);
7 - chart1 = plot(R, f1, '--', R, f2, R, f3, R(i), f1(i), 'k*', R(j), f1(j), 'k*');
8 - text(R(i)-0.25, f1(i)+0.015, ['R_1= ' num2str(R(i))]);
9 - text(R(j)-0.05, f1(j)+0.08, ['R_2= ' num2str(R(j)-0.001)]);
10 - chart1(3).LineWidth = 2;
11 - legend('R^3/8', 'c_1_2/c_1_1=0', 'c_1_2/c_1_1=0.5')
12
script Ln 11 Col 50

```

**Figure 20.** Code for solving intersection problem

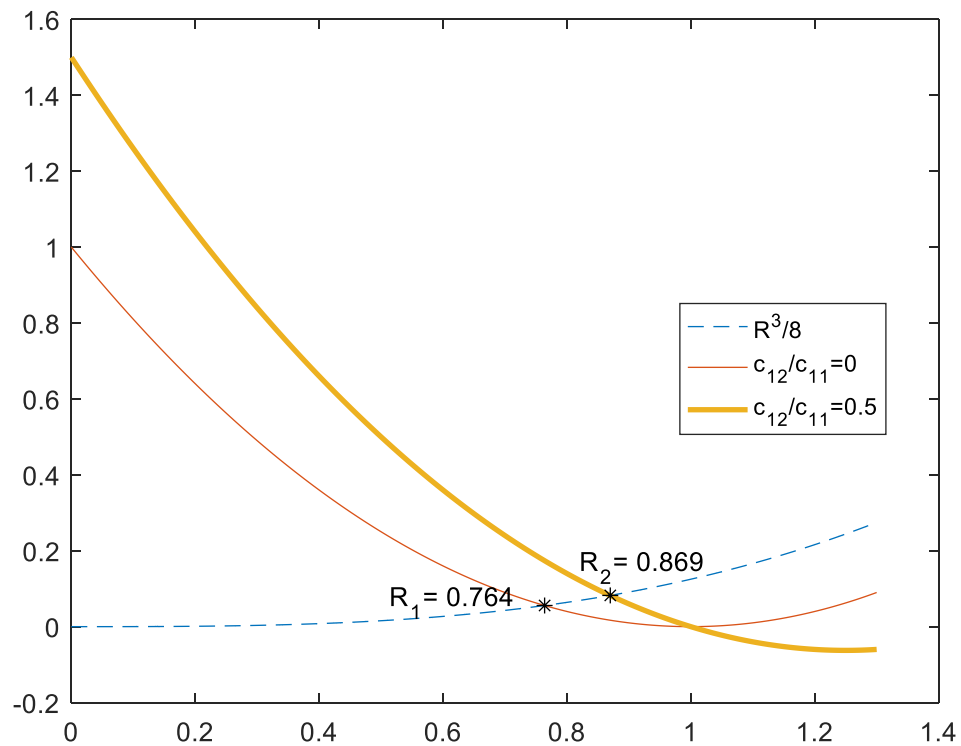


**Figure 21.** Plot for solving the Eq. (B-1)

As we can see from figure 21, when  $c_{12}/c_{11}$  running from 0 to 0.5, the curve of this function  $f_2(R)$  switches from the red curve (light solid curve) to the orange one (bold solid curve). The intersection between these curves and the blue dash curve is dynamic, moving from  $R_1$  to  $R_2$  accordingly. Thus, we can conclude that the positive real root of eq. (B-1) locates between 0.764 and 0.869, which means the ratio  $\frac{v_R}{v_t} = \sqrt{R}$  ranges from 0.874 to 0.9325 correspondingly.

## BIBLIOGRAPHY

- [1] E. Ghali, *Corrosion Resistance of Aluminum and Magnesium Alloys: Understanding, Performance, and Testing*. Hoboken: John Wiley & Sons, Inc., 2010.
- [2] J. Krautkrämer and H. Krautkrämer, “Ultrasonic testing,” pp. 1–36, 1990.
- [3] N. Suchato, A. Kalashnikov, R. Light, S. Sharples, and A. A. N. Corrosion, “Experimental Setup of Continuous Ultrasonic Monitoring for Corrosion Assessment,” pp. 2–5.
- [4] D. A. Russell, “Acoustics and Vibration Animations.”
- [5] E. A. Naryshkina, *General theory of Rayleigh waves for a half-space*, vol. No.90. 1940.
- [6] I. A. Viktorov, *Rayleigh and Lamb Waves*. New York: Plenum, 1967.
- [7] D. Royer and E. Dieulesaint, “Elastic Waves in Solids I Free and Guided Propagation.pdf.” 1996.
- [8] R. G. Leisure, “Ultrasonic spectroscopy : applications in condensed matter physics and materials science,” 2017.
- [9] J. F. Nye, “Physical properties of crystals : their representation by tensors and matrices,” 1979.
- [10] M. Levy *et al.*, “Handbook of Elastic Properties of Solids, Liquids, and Gases BOOK REVIEWS,” vol. 15, pp. 10–13, 2004.
- [11] R. A. Lemons and C. F. Quate, “Acoustic microscope—scanning version,” vol. 163, no. 1974, pp. 2–5, 2003.
- [12] A. Atalar, C. F. Quate, and H. K. Wickramasinghe, “Phase imaging in reflection with the acoustic microscope,” vol. 791, pp. 10–13, 1977.
- [13] W. Parmon and H. L. Bertoni, “Ray interpretation of the material signature in the acoustic microscope,” vol. 15, no. 21, 1979.
- [14] J. Kushibiki and N. Chubachi, “Material Characterization by Line-Focus-Beam Acoustic Microscope,” no. 2, 1985.

- [15] J. Kushibiki, A. Ohkubo, and N. Chubachi, "LINEARLY FOCUSED ACOUSTIC BEAMS FOR ACOUSTIC MICROSCOPY," vol. 17, no. 15, pp. 520–522, 1981.
- [16] K. Yamanaka, "Surface acoustic wave measurements using an impulsive converging beam," vol. 4323, 1983.
- [17] S. Lower, "Electrochemistry - Chemical reactions at an electrode, galvanic and electrolytic cells." 2004.
- [18] N. N. Hsu, D. Xiang, S. E. Fick, and G. V Blessing, "And polarization resolved ultrasonic measurements using a," pp. 867–871, 1995.
- [19] "Typical Material Properties of 420 Stainless Steel Infiltrated with Bronze."
- [20] D. Royer and E. Dieulesaint, "Elastic Waves in Solids I Free and Guided Propagation." 1996.
- [21] D. Chicot *et al.*, "Mechanical properties of magnetite (  $\text{Fe}_3\text{O}_4$  ), hematite (  $\alpha$  - $\text{Fe}_2\text{O}_3$  ) and goethite (  $\alpha$  - $\text{FeO} \cdot \text{OH}$  ) by instrumented ...," vol. 129, no. October 2011, 2015.
- [22] T. Bell, "Steel Grades and Properties What are the different types of steel" 2017. [Online]. Available: <https://www.thebalance.com/steel-grades-2340174>.